PNAS RESEARCH ARTICLE | CHEMISTRY

Particle-based hematite crystallization is invariant to initial particle morphology

Yining Wang[a,b,1], Sichuang Xue[a,1], Qingyun Lin[a,c,d,1], Duo Song[a], Yang He[a,e], Lili Liu[a], Jianbin Zhou[a], Meirong Zong[a], James J. De Yoreo[a,f], Junwu Zhu[b,2], Kevin M. Rosso[a,2], Maria L. Sushko[a,2], and Xin Zhang[a,2]

Edited by Lia Addadi, Weizmann Institute of Science, Rehovot, Israel; received July 9, 2021; accepted January 30, 2022

Understanding the mechanism of particle-based crystallization is a formidable problem due to the complexity of macroscopic and interfacial forces driving particle dynamics. The oriented attachment (OA) pathway presents a particularly challenging phenomenon because it occurs only under select conditions and involves a precise crystallographic alignment of particle faces often from distances of several nanometers. Despite the progress made in recent years in understanding the driving forces for particle face selectivity and alignment, questions about the competition between ion-by-ion crystallization, near-surface nucleation, and OA remain. This study examines hydrothermal conditions leading to apparent OA for hematite using three initial particle morphologies with various exposed faces. All three particle types formed single-crystal or twinned one-dimensional (1D) chain-like structures along the [001] direction driven by the attractive interactions between (001) faces and repulsive interactions between other pairs of hematite faces. Moreover, simulations of the potential of mean force for iron species and scanning transmission electron microscopy (S/TEM) imaging confirm that the formation of 1D chains is a result of the attachment of independently nucleated particles and does not follow the near-surface nucleation or ion-by-ion crystallization pathways. These results highlight that strong face specificity along one crystallographic direction can render OA to be independent of initial particle morphology.

oriented attachment (OA) | particle-based crystallization | hematite | nonclassical crystallization | interfacial force

Significance

Many crystallization processes occurring in nature produce highly ordered hierarchical architectures. Their formation cannot be explained using classical models of monomer-by-monomer growth. One of the possible pathways involves crystallization through the attachment of oriented nanocrystals. Thus, it requires detailed understanding of the mechanism of particle dynamics that leads to their precise crystallographic alignment along specific faces. In this study, we discover a particle-morphology–independent oriented attachment mechanism for hematite nanocrystals. Independent of crystal morphology, particles always align along the [001] direction driven by aligning interactions between (001) faces and repulsive interactions between other pairs of hematite faces. These results highlight that strong face specificity along one crystallographic direction can render oriented attachment to be independent of initial particle morphology.

As one of the most important physicochemical processes, crystallization plays key roles in geochemical and biological processes and in materials synthesis (1–11). With the development of *in situ* characterization and its expansion into more complex systems, numerous nonclassical crystallization phenomena, i.e., crystallization processes that do not involve monomer-by-monomer addition, were observed (3, 5, 6, 12–23). One of the common types of nonclassical crystallization pathways involves the repeated attachment of either crystalline or amorphous particles. Among various particle-based crystallization phenomena, oriented attachment (OA) of crystalline particles has attracted particular attention (14, 24–33). To date, OA has been observed in a wide range of synthetic systems and natural environments (3, 5, 6, 11, 12, 14, 15, 20, 24, 25). Moreover, OA has shown enormous potential in synthesizing single crystals with well-defined size and a wide variety of crystal morphologies including chains (34), nanorods (35, 36), nanosheets (37), nanocubes (38), nanowires (24, 39), nanobranches (40), and so on. Because single crystals with various unique morphologies emerge from self-assembled nanocrystals, OA has been widely used in various fields including energy storage (41, 42), catalysis (43–46), optics (47), and biomedicine (48, 49), to synthesize nanomaterials that exhibit superior functionality.

Although the idea of crystal growth via the attachment of aligned small crystals was first proposed more than 100 y ago (50, 51), a definitive proof of the OA pathway was obtained only recently by direct *in situ* observation of particle attachment in liquid cell transmission electron microscopy (TEM) (27, 52). These experiments revealed complex dynamic processes preceding attachment, encompassing small particle translation along the surface of the bigger particle; rotation; and, finally, alignment along the matching crystallographic face followed by a rapid jump to contact from about 1 nm distance (27, 52). This sampling of relative orientation of nanocrystals while in a long-lived solvent-separated state at distances of several nanometers points to a critical role of chemical dynamics at particle–solution interfaces, which produces the forces that attract, align, and attach specific crystal faces to each other.

This process of sequential particle attachment often produces one-dimensional (1D) single crystals or twinned chains. The pathway may be more complex when two- or three-dimensional (2 or 3D) architectures are formed. Based on cryogenic transmission

Author contributions: J.J.D.Y., J. Zhu, K.M.R., M.L.S., and X.Z. designed research; Y.W., S.X., Q.L., D.S., Y.H., L.L., J. Zhou, M.Z., M.L.S., and X.Z. performed research; Y.W., S.X., Q.L., D.S., J.J.D.Y., J. Zhu, K.M.R., M.L.S., and X.Z. analyzed data; and Y.W., S.X., Q.L., M.L.S., and X.Z. wrote the paper.

The authors declare no competing interest.

This article is a PNAS Direct Submission.

[1]Y.W., S.X., and Q.L. contributed equally to this work.

[2]To whom correspondence may be addressed. Email: xin.zhang@pnnl.gov, maria.sushko@pnnl.gov, kevin.rosso@pnnl.gov, or zhujw@njust.edu.cn.

This article contains supporting information online at http://www.pnas.org/lookup/suppl/doi:10.1073/pnas.2112679119/-/DCSupplemental.

Published March 11, 2022.

electron microscopy (cryo-TEM) time series, these structures have been proposed to form in a multistep process involving the formation of mesocrystals composed of oriented nanocrystals as a precursor (25). Moreover, recent *in situ* TEM studies revealed that the OA-like formation of 3D mesocrystals from saturated solutions can be mediated by the nucleation of new particles in the interfacial region of the existing particles followed by their subsequent attachment (31, 53). This recently identified pathway, in which nucleation and assembly processes are intimately linked, is distinct from the OA of independently nucleated particles (26, 52). Simulations predict that this pathway is driven by deviations in solution chemistry in the interfacial region near existing particles that reach a maximum at ∼1 to 2 nm distance from the particle surface, creating conditions for nucleation of new particles and attractive forces that drive the particles to attach to one another (31, 53). In contrast, numerous theoretical calculations and simulations predict that OA is driven by a balance of attractive and repulsive interparticle forces, some of which are mediated by interfacial solution structure (32, 52–55).

In light of the implication of OA in geochemistry and materials synthesis, considerable effort has been devoted to the understanding of the underlying mechanism and conditions favoring OA. Progress has been made in identifying the strength and range of the driving forces for facet-specific interparticle attraction. These studies have combined recent experimental methods for measuring orientation-specific interactions between nanocrystals and interfacial structure and dynamics with well-established and other modeling techniques (52, 56–60). The findings show that face specificity of attractive interparticle forces during the initial stages of approach from ∼6 to 8 nm is due to some combination of macroscopic dipole–dipole forces, shape-specific van der Waals interactions, and mesoscopic ion correlation interactions between ion density fluctuations in the electric double layers of the particles (52, 54, 55, 60–64). At closer separations of ∼1 to 6 nm the main forces driving facet specificity and alignment are dominated by the entropic hydration and ion correlation forces (52, 54, 55, 61). Chemical interactions, which encompass enthalpic hydration, and van der Waals interactions due to materials dielectric anisotropy dominate interparticle interactions at separations smaller than 1 nm (54). Finally, once in contact, reduction of surface energy drives chemical bonding between particle surfaces, thus completing the transformation into a single or twinned crystal. We note that particles are often already aligned before the jump to contact and attachment take place, as evidenced by *in situ* liquid cell TEM imaging of the OA process (27, 29, 30, 52).

Hematite (α-Fe_2O_3) is an important system for expanding understanding about conditions that select for OA versus ion-by-ion growth. Particle-based hematite crystallization has been reported widely, including formation of 1D chain-like structures to 3D superstructures (20, 34, 65). However, the underlying basis that selects one type of crystal architecture versus another remains poorly understood. While previous studies have focused on understanding facet selectivity and alignment between two particles, none have yet put this knowledge to the test by examining particle morphology effects on crystallization outcomes. Here we systematically investigated particle-based growth of hematite in hydrothermal suspensions of initial particles possessing three distinct morphologies: 1) rhombohedral particles with 6 {104} faces, 2) hexagonal nanoplates with {001} and {012} facets, and 3) hexagonal bipyramids with 12 {116} facets. High-resolution (HR) scanning transmission electron microscopy (S/TEM) studies show that, independent of initial particle morphology, their dominant attachment behavior always favors alignment along the [001] axis, yielding 1D chain structures. Theoretical calculations predict that this invariance in the attachment direction along [001] originates in the repulsive interactions between all other hematite face pairs studied.

Results and Discussion

Hematite nanoparticles with different morphologies (Fig. 1) were prepared using iron(III) chloride hexahydrate as iron source under hydrothermal or solvothermal conditions (see *Methods* for details). Surfactants were not used during synthesis to avoid surface modification with adsorbates. The morphology and structure of as-synthesized hematite nanoparticles were first characterized in detail using X-ray diffraction (XRD), scanning electron microscopy (SEM), and HR S/TEM. As shown in *SI Appendix*, Fig. S1, the XRD patterns indicated that all samples were pure hematite with high crystallinity. All diffraction patterns matched well with rhombohedral α-Fe_2O_3 (International Centre for Diffraction Data 33-0664) (66, 67). The sharp peaks located at the 2θ angles of 33.3°, 35.7°, and 54.2° were assignable to (104), (110), and (116) lattice planes, respectively.

SEM and TEM reveal the highly uniform particle sizes, shapes, and optimal crystallinity for each of the three types of morphologically distinct hematite nanoparticles (Fig. 1). Fig. 1*A* shows the hexagonal-shaped hematite nanoplatelets defined by 2 dominant {001} basal facets and 12 {012} edge facets, for which the surface area ratio of {001} to {012} is 52:48. The 3D schematic inserted in Fig. 1*A* illustrates the morphology of hexagonal-shaped hematite particles where blue represents {001} planes and green represents {012} planes. The HRTEM micrograph in Fig. 1*D* shows the high crystallinity of the nanoplatelets. Similar high-quality synthesis results were obtained for the other two sets of hematite particles. The second set consisted of rhombic crystals enclosed by 6 {104} facets shown in Fig. 1 *B* and *E*. The third set consisted of hexagonal bipyramidal particles enclosed by 12 {116} facets as shown in Fig. 1 *C* and *F*. The orientation of the enclosing facets was confirmed using HRTEM. For example, Fig. 1*F* confirms that (116) planes terminate the hexagonal bipyramidal particles by referencing to the [1-10] zone axis. More details of the characterization results are provided in *SI Appendix*, Figs. S2–S4.

To examine the aggregation behavior of the three nanoparticle types, we focused on hydrothermal conditions at temperatures between ∼120 and 180 °C, using various solutions ranging from pure water to dilute ferric chloride as an additional source of iron. Excess Fe was added either as ferric chloride salt hydrate or as akageneite (β-FeOOH) solids (*Methods*), which is a mineral phase more soluble than hematite. The concentration of the hematite nanoparticle suspension is 1.6 $mg \cdot mL^{-1}$ and the concentration of the additional iron source is up to 10 mM (defined as Fe concentration). The ferric chloride additive was used to understand the role of solubilized iron cations on growth by particle attachment, particularly as a consequence of changes in the ion correlation force. Depending on the form of the ferric chloride used (*Methods*), the initial pH of the solutions ranged from ∼3 to 6. These weakly acidic conditions enable solubilization of the ferric chloride additive while avoiding dissolution of the hematite nanoparticles.

First, we explored the aggregation behavior of the hexagonal-shaped hematite nanoplatelets. In pure water at 180 °C, no

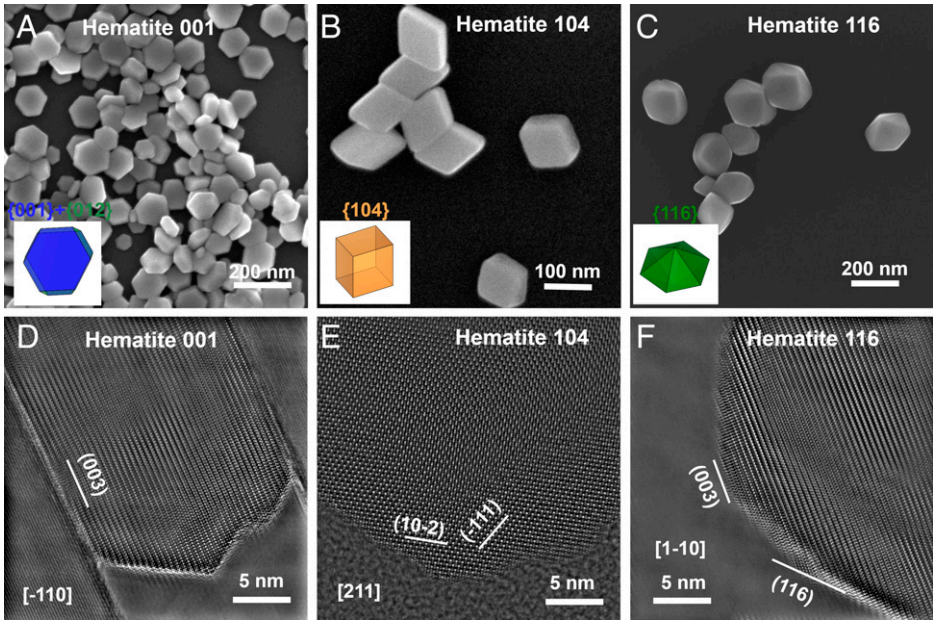

Fig. 1. The morphologies of the three sets of initial as-synthesized hematite nanoparticles. (*A* and *D*) Hexagonal-shaped nanoplatelets with 2 {001} basal facets and 12 {012} edge facets. (*B* and *E*) Rhombic-shaped nanoparticles with 6 {104} facets. (*C* and *F*) Hexagonal bipyramid-shaped nanoparticles with 12 {116} facets.

particle aggregation was observed despite being held at these conditions for 2 d (*SI Appendix*, Fig. S5 *A* and *B*). However, in the presence of additional iron sources, such as 5 mM akageneite (defined as the concentration of Fe ions in the solution after dissolving the solid completely), multiparticle crystals were observed after 2 d. This indicates the importance of excess free Fe^{3+} ions in driving particle-based crystallization in the hematite system (*SI Appendix*, Fig. S5 *C–F*). The resulting multiparticle crystals were composed of multiple hexagonal-shaped hematite nanoplates aligned along the [001] axis to form a chain, with interparticle boundaries either lattice matched or related through twinning (Fig. 2**)**. The single-crystal nature of these multiparticle chains was confirmed using selected area electron diffraction (SAED) (a corresponding fast Fourier transform [FFT] pattern is shown in Fig. 2 *B*, *Inset*). The single-crystal or twinned nature of the boundaries was verified by the mutual orientation of the (104) and (012) planes of the neighboring nanoplates (Fig. 2 *B* and *C*). For example, the twinning angle between the (012) edge planes in two adjacent crystals in Fig. 2 was 115.52° along the zone axis [010] in both images. All diffraction spots in the FFT pattern shown in Fig. 2*D* can be identified as twin and matrix. The corresponding FFT patterns for both regions of Fig. 2*C* reveal that the twin boundary is parallel to the (006) plane.

Remarkably, we found that the propensity of hematite nanoparticles to form chain-like structures along the [001] direction was found to be invariant to the initial nanoparticle morphology and synthesis temperature. For example, after aging the rhombic-shaped nanoparticles at 120 °C for 7 d, *ex situ* S/TEM revealed formation of 1D chain-like structures composed of two to seven rhombic-shaped nanoparticles aligned along [001] (Fig. 3 *A–C* and *SI Appendix*, Figs. S6 *A–E* and S7). The lattice-matched boundary between rhombic grains is consistent with high crystallinity within the multiparticle array (Fig. 3*B*), and this was further confirmed using SAED (Fig. 3 *B*, *Inset*). The mutual orientation between the (104) and (012) planes of neighboring particles measured using HRTEM imaging and SAED clearly point to their alignment along the [001] direction. When the temperature of hydrothermal aging was increased to 180 °C, the rhombic particles evolved into hexagonal bipyramidal shapes (*SI Appendix*, Figs. S6 *F–H* and S8) including partial exposure of {113} facets (*SI Appendix*, Fig. S8*C*). This local reconstruction can be attributed to the instability of {104} planes relative to the nanoplatelet morphology as well as {113} facets at the higher-temperature condition. Nonetheless, in all cases explored, the rhombic nanoparticles merged along the [001] direction, similar to the hexagonal nanoplatelets (*SI Appendix*, Fig. S8 *A* and *B*).

Finally, similar 1D arrays were observed for the hexagonal bipyramidal particles with 12 {116} facets in the presence of excess iron at 120 °C (Fig. 3 *D–F* and *SI Appendix*, Fig. S9 *A–E*). As presented in Fig. 3*E*, the lattice-matched boundary between two particles was observed via HRTEM imaging using reference orientations of (110) and (003) planes of neighboring particles (Fig. 3 *E*, *Inset*). Qualitatively similar array formation along [001] was also obtained at a higher temperature of 180 °C (*SI Appendix*, Figs. S9 *F–H* and S10). However, here again the relative instability of {116} facets was evident from the emergence of {113} facets. The structures of the aggregates were further explored using 3D tomographic reconstruction. S/TEM-high-angle annular dark-field (HAADF) micrographs were collected every 2° between −70° and +70° along the α-axis of the holder and combined to construct 3D tomographs showing the morphology of chain-like aggregates of hematite {116} nanoparticles (*SI Appendix*, Figs. S11 and S12).

The consistency of the observed aggregation along [001] independent of the initial particle morphology points to a uniform mechanism of alignment. Although the presence of excess iron is important for mediating aggregation, complete reformation by simple ion-by-ion recrystallization can be ruled out given that initial particle morphologies are largely preserved. Hence this mechanism may involve either 1) OA of independently nucleated particles or 2) preferential nucleation of new particles in the interfacial region at the (001) surface of the existing particles followed by either jump to contact or attachment via bridge formation (3).

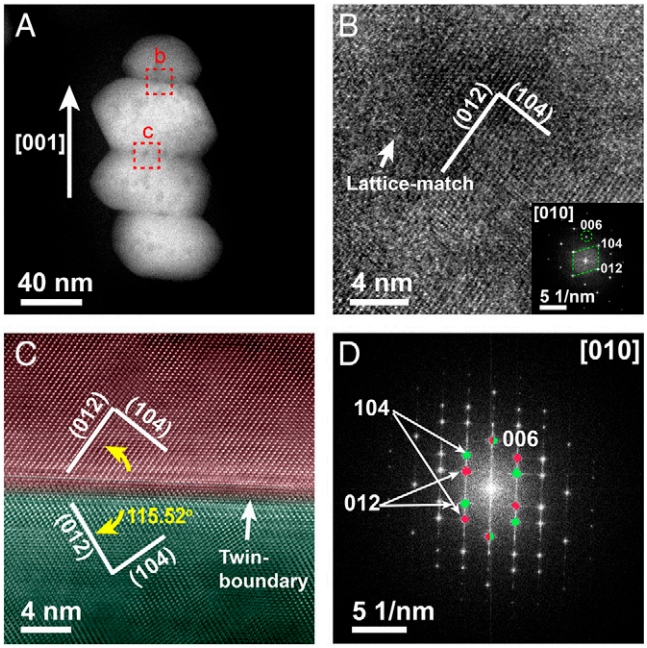

Fig. 2. Multiparticle chains formed from hematite nanoplatelets possessing {001} and {012} facets after hydrothermal aging in the presence of excess iron at 180 °C. (*A*) Low-magnification HAADF image showing the aggregation of the hematite nanoplates. (*B*) HRTEM image of the lattice-matched particle boundary, marked with a red dashed box in *A*. *Inset* is the corresponding FFT pattern. (*C*) HRTEM image of the particles with twin boundary, marked with a red dashed box in *A*. (*D*) Corresponding FFT pattern of *C*. The red pattern corresponds to the upper particle, while the green one corresponds to the lower particle.

To delineate between these two scenarios theoretical simulations of interparticle forces and the potential of mean force (PMF) of iron species at various hematite faces were performed. Simulations were performed using classical density functional theory (cDFT) in an aqueous solution of 10 mM $FeCl_3$, pH 3, at 120 °C and explored forces in the electric double layer (EDL) and the EDL-mediated forces between two particles separated by ∼0.5 to 8 nm. The structure of hydroxylated hematite facets and their relative surface energies were determined using plane-wave DFT, which informed cDFT simulations (31, 52, 61). Simulations of interparticle forces revealed high-energy barriers preventing aggregation between two {012} and two {104} faces (Fig. 4). In contrast, the calculated distance dependence of the disjoining pressure between two {001} hematite surfaces has a profile typical of the systems undergoing OA. Specifically, the force–distance curve has a deep primary minimum at close separations and two shallow secondary minima at separations of 1.5 and 3.5 nm (Fig. 4). The barriers between secondary minima are of the order of ∼5 kT/nm^2, which is expected to temporarily slow down particle approach, but allow for thermally induced transitions between the metastable states. As we have shown in our previous work, particles can undergo rotation around the [001] axis for fine adjustment of their mutual orientation toward lattice matching or twinned configuration while in the metastable states (61). The combination of long-range facet selectivity and fine-aligning forces rotating the {001} faces to lattice-matching or twinned configurations provides a pathway for 1D array formation by independently nucleated particles. It is noteworthy that the theoretical approach used here provides information on interparticle forces for particles separated by at least one layer of "liquid" water, i.e., water that is not physi/chemisorbed onto particles' surfaces. When the attachment is not prohibited by energy barriers in the solvent-separated state, the next stages of particle attachment involve elimination of interfacial hydroxyl groups and chemical bonding between two particles. The mechanism of these processes remains poorly understood and requires further careful study. One of the proposed models involves a zipper-like mechanism, in which consecutive recombination of surface hydroxyls with protons and their elimination from the gap create the conditions for direct interparticle binding (28). We

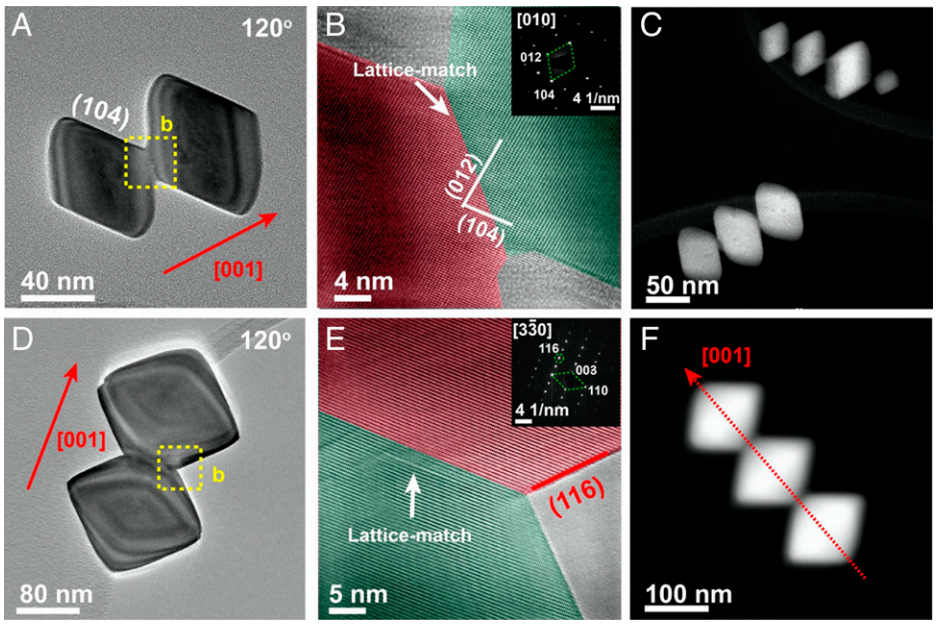

Fig. 3. Oriented attachment of rhombic nanoparticles with 6 {104} facets (*A*–*C*) and hexagonal bipyramidal nanoparticles with 12 {116} facets (*D*–*F*) at 120 °C. (*A*) Low-magnification TEM image of an aggregated hematite dimer with {104} facets at 120 °C. (*B*) HRTEM image, showing the lattice-matched particles boundary, marked by a yellow dashed box in *A*. *Inset* is the corresponding SAED pattern. (*C*) Low-magnification HAADF image, showing the morphology of the aggregated α-Fe_2O_3 nanoplates. (*D*) Low-magnification TEM image, showing the hematite dimer of {116} nanocrystals formed at 120 °C. (*E*) HRTEM image, showing the lattice-matched particles boundary, marked by a yellow dashed box in *D*. *Inset* is the corresponding SAED pattern. (*F*) Low-magnification HAADF image of a hematite trimer.

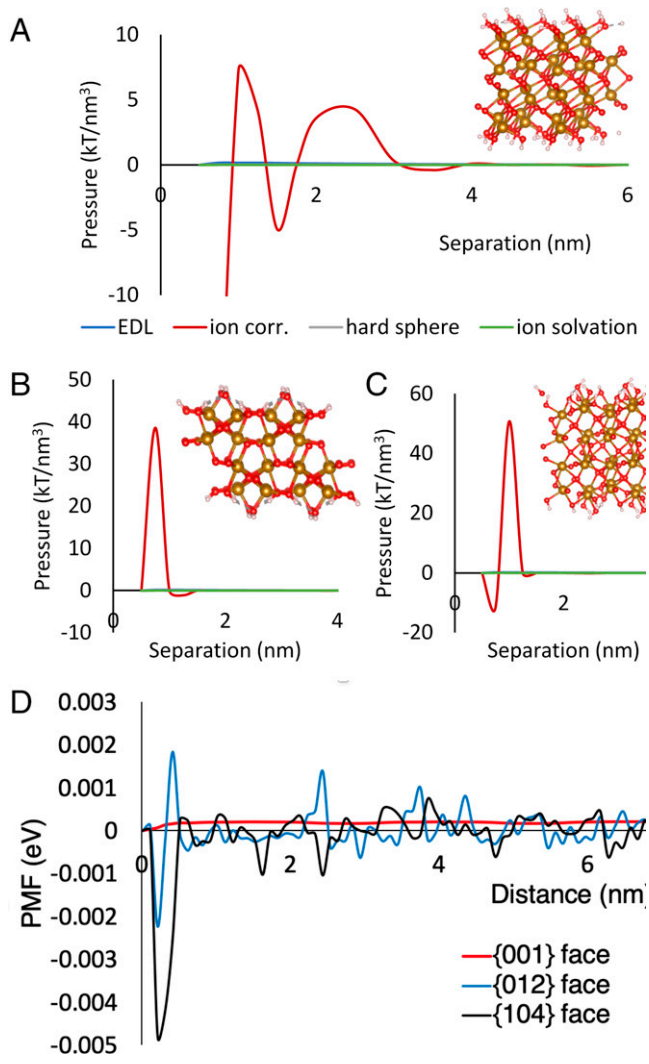

Fig. 4. The driving forces for hematite 1D array formation. (*A–C*) Interactions between (*A*) two {001}, (*B*) two {012}, and (*C*) two {104} hematite faces. The components of interparticle forces are shown as blue lines for EDL forces, red lines for ion correlation forces, gray lines for hard sphere excluded volume interactions, and green lines for ion solvation interactions. *Insets* in *A–C* show the structure of hydroxylated hematite faces. (*D*) The PMF of iron species at {001} (red line), {012} (blue line), and {104} (black line) surfaces.

anticipate that these processes will give rise to another energy barrier due to enthalpic hydration interactions at about 0.3 nm separation followed by a deep energy minimum at particle contact. However, the presented theoretical model cannot quantify this barrier.

Simulations predict that for all pairs of crystal faces studied the disjoining pressure is dominated by mesoscopic ion-correlation forces, which are the van der Waals forces due to the interactions between the instantaneous dipoles in the opposing EDLs (Fig. 4). Ion fluctuation dynamics in the EDL are very sensitive to the distribution of hydroxyl groups on a mineral surface (18, 31, 52, 54, 61), which, in turn, depends on the crystal face and solution pH, thereby providing the mechanism for facet selectivity and alignment during the OA process. It is noteworthy that ion correlation interactions also strongly depend on the concentration of excess electrolyte. Namely, the more diffuse is the EDL, the weaker are the correlations between ionic fluctuations. For example, at $FeCl_3$ concentration of 2 mM the EDL becomes too diffuse for correlated ion fluctuation dynamics and ion correlation interactions between {001} surfaces become negligibly small (*SI Appendix*, Fig. S13). At this excess iron concentration, the interactions between {001} surfaces are dominated by Coulomb repulsion and particles are predicted not to attach, as observed experimentally in the low excess iron regime.

To evaluate the feasibility of the near-surface nucleation pathway, the interfacial forces acting on iron species were analyzed. The PMF curves for iron species indicate that there is no driving force for particles to nucleate in the interfacial region (Fig. 4*D*). Despite the differences in the PMF profiles, at all three hematite faces the PMFs of iron species are either purely repulsive, as at the {001} surface, or attractive only in the immediate vicinity of the surface, as at {104} and {012} faces. These PMFs are therefore inconsistent with the near-surface nucleation pathway, but support growth by monomer addition. The PMF data suggest that the probability of classical growth by monomer addition is the highest at {104} faces and the lowest at the {001} face, which is consistent with the observed relative stabilities of these surfaces deduced from the microscopic observations and first-principles simulations. In particular, DFT calculations for the vacuum-terminated surfaces predict that the surface energy of the {001} face is the lowest and equal to 149.8 meV/Å^2 while the surface energies of {104} and {012} faces in vacuum are 271.5 and 158.4 meV/Å^2, respectively, suggesting that the {001} surface is the most stable. Overall, simulations of the PMFs and the face-specific interparticle interactions point to the OA mechanism for the formation of 1D hematite arrays.

It is noteworthy that the formation of particle-based regular architectures through OA, in which particles form single-crystal or twinned hierarchical structures, can be driven by macroscopic interparticle forces and/or interactions between opposing EDLs at particle surfaces (54). Often these forces work in tandem to direct face-specific particle orientation, alignment, and attachment (52). Bulk hematite is weakly ferromagnetic; thereby it is conceivable that even in the absence of external magnetic-field interactions between the magnetic dipoles of hematite, particles may contribute to their alignment during the formation of the chain-like structures. Extensive studies of hematite particles assembly demonstrated that magnetic forces on their own cannot drive the formation of 1D, 2D, or 3D architectures, but it is imperative that magnetic forces are coupled with morphology-specific steric interactions to drive the assembly (68–72). In this study, the central conclusion is reversed. That is, 1D chains form along the [001] direction independent of particle morphology. However, the OA takes place only when the concentration of excess Fe^{3+} is no smaller than 5 mM. The excess Fe^{3+} concentration threshold marks the concentration of ions in the electric double layer sufficient to give rise to attractive ion-correlation forces between {001} hematite faces exceeding several kT (Fig. 4*A*) and thereby driving particle alignment and attachment. The contribution of macroscopic magnetic and van der Waals interactions and associated torque was found to be of the order of 0.01 and 0.5 kT, respectively, which is more than an order of magnitude smaller than that of ion-correlation interactions (*SI Appendix* and *SI Appendix*, Fig. S14). Therefore, magnetic torque is insignificant compared to stochastic Brownian forces and is unlikely to affect particle alignment in the absence of applied magnetic field.

In conclusion, our study revealed the remarkable independence of hematite particle assembly behavior on particle morphology at hydrothermal conditions. We found that, independent of nanoparticle shape and the nature of the exposed

crystal faces, in the presence of excess iron hematite nanoparticles assemble into chain-like 1D arrays aligned along the [001] direction. Theoretical simulations of interparticle forces and the PMF of the iron species predict [001] array formation through the OA mechanism, as opposed to near-surface nucleation, driven by face-specific ion correlation forces. On the one hand these simulations predict long-range attraction between {001} hematite faces and the presence of two metastable states facilitating particle alignment and high repulsive barriers preventing particle aggregation along {104} and {012} faces. On the other hand, the PMF of iron species is inconsistent with the near-surface nucleation pathway for array formation. The combined experimental observations and theoretical predictions highlight aspects of the OA mechanism that strong face specificity along one crystallographic direction can render the OA to be independent of particle morphology. The findings thus provide insights for understanding the formation of certain unique crystallization patterns observed in natural systems, in this case particularly 1D structures such as those observed in the growth of microplaty hematite crystallites that comprise nano- or microsized particles in hematite ores located at Hamersley Province, Australia (11). They also provide a basis for understanding the formation of oriented biominerals (e.g., modern and fossil nacre from molluscans) (73) and nanowires/chains/rods/needles [e.g., PbSe (74), CdSe (75), ZnO (35, 52), and hematite 1D materials (34)] with particle-based morphologies.

Methods

1. **Chemicals and Materials.** Iron(III) chloride hexahydrate ($FeCl_3{\cdot}6H_2O$, 97%) was purchased from Sigma Aldrich Chemical Reagent Co., Ltd. Sodium acetate ($CH_3COONa{\cdot}3H_2O$, pure) was purchased from Amresco Chemical Reagent Co., Ltd. Ethanol (200 proof) was purchased from Decon Laboratories. All chemicals are analytical purity and can be used directly without any further treatment. Deionized (DI) water used in this work was made with a Barnstead water purification system.

2. **Materials Synthesis.**
   - ***2.1. Synthesis of hexagonal-shaped hematite nanoplates.*** The hexagonal-shaped hematite nanoplates were synthesized based on the method in ref. 20. In brief, 270.3 mg $FeCl_3{\cdot}6H_2O$ was dissolved in a mixed solution (10 mL, $V_{ethanol}/V_{water}$ is 9:1) under magnetic stirring at room temperature to form a 0.1-M homogeneous solution. Then, 1.3276 g of sodium acetate was slowly introduced into the above suspension with stirring. After stirring at room temperature for about 6 h, the obtained mixture was transferred into a 20-mL Teflon liner stainless steel autoclave and held at 180 °C for 12 h. After washing with DI water several times, the final hexagonal-shaped products with {001} and {012} facets were collected by centrifugation at 8,000 rpm.
   - ***2.2. Synthesis of rhombic-shaped hematite nanoplates.*** A total of 27.0 mg $FeCl_3{\cdot}6H_2O$ was dissolved into 10 mL DI water at room temperature to form a 10-mM homogeneous solution. Then, the obtained solution was transferred into a 20-mL Teflon liner stainless steel autoclave and heated at 120 °C for 3 d. After washing with DI water several times and centrifugation at 8,000 rpm, the final rhombic-shaped products with 6 {104} facets were collected.
   - ***2.3. Synthesis of hexagonal bipyramid-shaped hematite nanocrystals.*** A total of 67.6 mg $FeCl_3{\cdot}6H_2O$ was dissolved into 10 mL DI water at room temperature to form a 25-mM homogeneous solution. Then, the obtained solution was transferred into a 20-mL Teflon liner stainless steel autoclave, put into an oven equipped with a rotation rack (10 rpm), and heated at 120 °C for 3 d. After washing with DI water several times and centrifugation at 8,000 rpm, the final hexagonal bipyramid-shaped products with 12 {116} facets were acquired.

3. **Aggregation Experiments.**
   - ***3.1. Synthesis of 1D arrays of hexagonal-shaped hematite nanoplates.*** Following the same process as in *2.1. Synthesis of hexagonal-shaped hematite nanoplates*, wet hexagonal-shaped hematite nanoplates with {001} and {012} facets were collected. The obtained wet powder was dispersed into 10 mL DI water to make the hematite (001) suspension for the aggregation studies. For the aggregation experiments in pure water, 1 mL of above-prepared hematite (001) suspension was diluted to 10 mL. For the aggregation experiments with additional iron sources, 1 mL of above-prepared hematite (001) suspension was diluted to 5 mL and then mixed with 5 mL 10 mM akaganeite (β-FeOOH) suspensions. The final concentration of the hematite nanoparticles and the additional iron source is 10 mM and 5 mM (both defined as Fe concentration), respectively. The fresh 10-mM akaganeite suspension was prepared via dispersing 89 mg akaganeite powder into 10 mL DI water. Then, the obtained suspension (10 mL pure hematite suspension or 10 mL hematite plus akaganeite suspension) was transferred into a 20-mL Teflon liner stainless steel autoclave and was kept at 180 °C for 2 d. After washing with DI water several times, the final chain-like hexagonal-shaped hematite nanoplates were collected by centrifugation at 8,000 rpm.
   - ***3.2. Synthesis of 1D arrays of rhombic-shaped hematite nanoplates.*** A total of 27.0 mg $FeCl_3{\cdot}6H_2O$ was dissolved into 10 mL of DI water at room temperature to form a homogeneous solution. Then, the obtained solution was transferred into a 20-mL Teflon liner stainless steel autoclave and held at 120 °C for 7 d or 120 °C for 3 d followed with 180 °C for 4 d. After washing with DI water several times and centrifugation at 8,000 rpm, the final chain-like rhombic-shaped products were collected.
   - ***3.3. Synthesis of 1D arrays of hexagonal bipyramid-shaped hematite nanocrystals.*** A total of 67.6 mg $FeCl_3{\cdot}6H_2O$ was dissolved into 10 mL DI water at room temperature to form a 25-mM homogeneous solution. Then, the obtained solution was transferred into a 20-mL Teflon liner stainless steel autoclave, put into an oven equipped with a rotation rack (10 rpm), and kept at 120 °C for 7 d or 120 °C for 3 d followed with 180 °C for 4 d. After washing with DI water several times and centrifugation at 8,000 rpm, the final chain-like hexagonal bipyramid-shaped samples were prepared.

4. **Characterization.** Powder XRD of all as-prepared samples was performed on a Philips X'pert Multi-Purpose Diffractometer (MPD) (PANAlytical) equipped with Cu Kα radiation operating at 50 kV and 40 mA within the 2θ range from 5° to 75°. SEM imaging was conducted on the FEI Helios NanoLab 600i dual-beam focused ion beam precision manufacturing instrument operating at 5 kV. Before SEM imaging, a thin carbon layer (about 5 nm) was deposited on the particle surface by using a carbon coater (208C; Ted Pella, Inc.) to improve the electronic conductivity of the samples.

The sample water suspensions were dusted on the holey carbon-coated copper grids (Lacey Carbon, 300 mesh; Ted Pella, Inc.) for subsequent microanalysis. The TEM investigation was performed in the FEI Titan 80-300 Environmental TEM microscope with an objective lens corrector and the FEI Titan 80-300 S/TEM microscope at 300 kV. The S/TEM microscope was equipped with a probe spherical aberration corrector that enabled subangstrom imaging using STEM-HAADF detectors and a Bruker energy dispersive X-ray spectrometer for element analysis. For STEM-HAADF imaging, the inner and outer collection angles of the annular dark-field detector were set at 55 and 220 mrad, respectively. The STEM-HAADF images for 3D tomography were collected every 2° from −70° to +70°. The 3D reconstruction was performed using TomViz.

5. **Simulation Methods.**
   - ***5.1. Plane-wave DFT.*** All DFT (76) geometry optimizations in this study were performed with the pseudopotential NWChem plane-wave (NWPW) module (77) implemented in the NWChem software package (78, 79). The Perdew–Burke–Ernzerhof (PBE) functional (80) was used to account for the exchange correlation energy. The on-site Coulombic (U) and exchange (J) constants were introduced in the energy functional (81) to correct the electron self-interaction error implicit in DFT calculations. In this work, U and J were chosen as 4 and 1 eV, respectively, which were found by comparing the DFT+U calculated properties using

different values (band gap, local spin moment, unit cell volume, etc.) with experimental results (82). These parameters were applied to the d-orbitals of the iron elements. In our plane-wave calculations, the valence electron interactions with the atomic core were approximated with generalized norm-conserving Hamann pseudopotentials (83) for O and H, and a norm-conserving Troullier–Martins pseudopotential (84), which contains 4s, 4p, and 3d projectors and a semicore correction, was applied for Fe. All the pseudopotentials were modified to the separable form suggested by Kleinman and Bylander (85). Unrestricted calculations were performed to accommodate spin ordering in the system. The electronic wavefunctions were expanded using a plane-wave basis with periodic boundary conditions at the Γ-point with a wavefunction cutoff energy of 100 Ry and a density cutoff energy of 200 Ry.

5.2. cDFT. The focus of the theoretical simulations was on understanding the thermodynamic driving forces for the observed nonclassical nucleation and growth pathway. To achieve this goal, we used a DFT-based atomistic-to-mesoscale approach we developed (61). The details of the cDFT approach used in this work were previously published elsewhere (see ref. 61 for full details and ref. 86 for numerical implementation) and are provided in *SI Appendix* for completeness. The aqueous salt solution was modeled as a dielectric medium with 78.5, consisting of discrete charged spherical particles representing ions and neutral spherical particles representing water molecules. The concentration of spherical "water molecules" was 55.5 M, chosen to model experimental water density. We used experimental crystalline ionic diameters for mobile ions equal to 0.146 nm for Fe^{3+}, 0.200 nm for H^+, and 0.275 nm for HO^- and van der Waals diameter for water molecules equal to 0.275 nm. Ion charges reflected the formal charges of ionic species and were equal to −1 for OH^-, +1 for H^+, +3 for Fe^{3+} ions, and 0 for water. The complexation between these species, e.g., Fe^{3+} and OH^-, in solution was not imposed a priori. However, the formation of multispecies complexes through electrostatic and short-range interactions may occur as a result of optimization of the structure of interfacial solution. Atomic positions of the surface atoms were used to define the spatial distribution of surface OH groups. Experimental enthalpies of hydration were used for short-range interactions of all ions with water. The model considers two hematite nanoparticles in aqueous solution containing 10 mM $FeCl_3$, pH 3, at interparticle separations varying from 0.5 to 7.0 nm. The temperature was 120 °C.

Data Availability. All study data are included in this article and/or *SI Appendix*.

ACKNOWLEDGMENTS. This work was supported by the US Department of Energy (DOE), Office of Science, Office of Basic Energy Sciences, Chemical Sciences, Geosciences, and Biosciences Division through its Geosciences Program at Pacific Northwest National Laboratory (PNNL). A portion of the work was performed using the Environmental and Molecular Sciences Laboratory, a national scientific user facility at PNNL sponsored by the DOE's Office of Biological and Environmental Research. PNNL is a multiprogram national laboratory operated by Battelle Memorial Institute under Contract DE-AC05-76RL01830 for the DOE. Y.W. thanks the China Scholarship Council for the financial support during her studies in the United States.

Author affiliations: [a]Physical & Computational Science Directorate, Pacific Northwest National Laboratory, Richland, WA 99354; [b]Key Laboratory for Soft Chemistry and Functional Materials, Ministry of Education, Nanjing University of Science and Technology, Nanjing 210094, China; [c]Center of Electron Microscopy, School of Materials Science and Engineering, Zhejiang University, Hangzhou 310027, China; [d]State Key Laboratory of Silicon Materials, School of Materials Science and Engineering, Zhejiang University, Hangzhou 310027, China; [e]Beijing Advanced Innovation Center for Materials Genome Engineering, University of Science and Technology Beijing, Beijing 10083, China; and [f]Materials Science and Engineering, University of Washington, Seattle, WA 98195

1. J. J. De Yoreo, P. G. Vekilov, Principles of crystal nucleation and growth. *Rev. Mineral. Geochem.* **54**, 57 (2003).
2. Q. Hu *et al.*, The thermodynamics of calcite nucleation at organic interfaces: Classical vs. nonclassical pathways. *Faraday Discuss.* **159**, 509–523 (2012).
3. J. J. De Yoreo *et al.*, CRYSTAL GROWTH. Crystallization by particle attachment in synthetic, biogenic, and geologic environments. *Science* **349**, aaa6760 (2015).
4. L. Liu, S. Zhang, M. E. Bowden, J. Chaudhuri, J. J. D. Yoreo, In situ TEM and AFM investigation of morphological controls during the growth of single crystal $BaWO_4$. *Cryst. Growth Des.* **18**, 1367–1375 (2017).
5. R. L. Penn, J. F. Banfield, Morphology development and crystal growth in nanocrystalline aggregates under hydrothermal conditions-insights from titania. *Geochim. Cosmochim. Acta* **63**, 1549–1557 (1999).
6. J. F. Banfield, S. A. Welch, H. Zhang, T. T. Ebert, R. L. Penn, Aggregation-based crystal growth and microstructure development in natural iron oxyhydroxide biomineralization products. *Science* **289**, 751–754 (2000).
7. A. J. Giuffre, A. C. Gagnon, J. J. De Yoreo, P. M. Dove, Isotopic tracer evidence for the amorphous calcium carbonate to calcite transformation by dissolution–reprecipitation. *Geochim. Cosmochim. Acta* **165**, 407–417 (2015).
8. X. Zhang, B. L. Weeks, Tip induced crystallization lithography. *J. Am. Chem. Soc.* **136**, 1253–1255 (2014).
9. F. Bai, K. Bian, X. Huang, Z. Wang, H. Fan, Pressure induced nanoparticle phase behavior, property, and applications. *Chem. Rev.* **119**, 7673–7717 (2019).
10. L. Meng *et al.*, Shape dependence of pressure-induced phase transition in CdS semiconductor nanocrystals. *J. Am. Chem. Soc.* **142**, 6505–6510 (2020).
11. M. S. Egglseder *et al.*, Tiny particles building huge ore deposits–Particle-based crystallisation in banded iron formation-hosted iron ore deposits (Hamersley Province, Australia). *Ore Geol. Rev.* **104**, 160–174 (2019).
12. R. L. Penn, J. F. Banfield, Imperfect oriented attachment: Dislocation generation in defect-free nanocrystals. *Science* **281**, 969–971 (1998).
13. M. H. Nielsen *et al.*, Investigating processes of nanocrystal formation and transformation via liquid cell TEM. *Microsc. Microanal.* **20**, 425–436 (2014).
14. H. Cölfen, M. Antonietti, Mesocrystals: Inorganic superstructures made by highly parallel crystallization and controlled alignment. *Angew. Chem. Int. Ed. Engl.* **44**, 5576–5591 (2005).
15. C. Rodríguez-Navarro, E. Ruiz-Agudo, J. Harris, S. E. Wolf, Nonclassical crystallization in vivo et in vitro (II): Nanogranular features in biomimetic minerals disclose a general colloid-mediated crystal growth mechanism. *J. Struct. Biol.* **196**, 260–287 (2016).
16. M. Jehannin, A. Rao, H. Cölfen, New horizons of nonclassical crystallization. *J. Am. Chem. Soc.* **141**, 10120–10136 (2019).
17. F. Yan *et al.*, Controlled synthesis of highly-branched plasmonic gold nanoparticles through peptoid engineering. *Nat. Commun.* **9**, 2327 (2018).
18. L. Liu *et al.*, Revisiting the growth mechanism of hierarchical semiconductor nanostructures: The role of secondary nucleation in branch formation. *J. Phys. Chem. Lett.* **10**, 6827–6834 (2019).
19. Z. Liu *et al.*, Shape-preserving amorphous-to-crystalline transformation of $CaCO_3$ revealed by in situ TEM. *Proc. Natl. Acad. Sci. U.S.A.* **117**, 3397–3404 (2020).
20. M. Zong *et al.*, Synthesis of 2D hexagonal hematite nanosheets and the crystal growth mechanism. *Inorg. Chem.* **58**, 16727–16735 (2019).
21. H. Fan, J. Gabaldon, C. J. Brinker, Y. B. Jiang, Ordered nanocrystal/silica particles self-assembled from nanocrystal micelles and silicate. *Chem. Commun. (Camb.)* **2006**, 2323–2325 (2006).
22. W. Wei, F. Bai, H. Fan, Oriented gold nanorod arrays: Self-assembly and optoelectronic applications. *Angew. Chem. Int. Ed. Engl.* **58**, 11956–11966 (2019).
23. Z. Zhao *et al.*, Phase control of hierarchically structured mesoporous anatase TiO_2 microspheres covered with {001} facets. *J. Mater. Chem.* **22**, 21965–21971 (2012).
24. K. S. Cho, D. V. Talapin, W. Gaschler, C. B. Murray, Designing PbSe nanowires and nanorings through oriented attachment of nanoparticles. *J. Am. Chem. Soc.* **127**, 7140–7147 (2005).
25. V. M. Yuwono, N. D. Burrows, J. A. Soltis, R. L. Penn, Oriented aggregation: Formation and transformation of mesocrystal intermediates revealed. *J. Am. Chem. Soc.* **132**, 2163–2165 (2010).
26. H. G. Liao, L. Cui, S. Whitelam, H. Zheng, Real-time imaging of Pt_3Fe nanorod growth in solution. *Science* **336**, 1011–1014 (2012).
27. D. Li *et al.*, Direction-specific interactions control crystal growth by oriented attachment. *Science* **336**, 1014–1018 (2012).
28. M. Raju, A. C. van Duin, K. A. Fichthorn, Mechanisms of oriented attachment of TiO_2 nanocrystals in vacuum and humid environments: Reactive molecular dynamics. *Nano Lett.* **14**, 1836–1842 (2014).
29. Z. Aabdin *et al.*, Bonding pathways of gold nanocrystals in solution. *Nano Lett.* **14**, 6639–6643 (2014).
30. C. Zhu *et al.*, In-situ liquid cell transmission electron microscopy investigation on oriented attachment of gold nanoparticles. *Nat. Commun.* **9**, 1–7 (2018).
31. G. Zhu *et al.*, Self-similar mesocrystals form via interface-driven nucleation and assembly. *Nature* **590**, 416–422 (2021).
32. X. Zhang *et al.*, Direction-specific van der Waals attraction between rutile TiO_2 nanocrystals. *Science* **356**, 434–437 (2017).
33. G. Mirabello *et al.*, Crystallization by particle attachment is a colloidal assembly process. *Nat. Mater.* **19**, 391–396 (2020).
34. L.-r. Meng *et al.*, Uniform α-Fe_2O_3 nanocrystal moniliforme-shape straight-chains. *Cryst. Growth Des.* **10**, 479–482 (2010).
35. C. Pacholski, A. Kornowski, H. Weller, Self-assembly of ZnO: From nanodots to nanorods. *Angew. Chem. Int. Ed. Engl.* **41**, 1188–1191 (2002).
36. B. Ludi, M. J. Süess, I. A. Werner, M. Niederberger, Mechanistic aspects of molecular formation and crystallization of zinc oxide nanoparticles in benzyl alcohol. *Nanoscale* **4**, 1982–1995 (2012).
37. C. Schliehe *et al.*, Ultrathin PbS sheets by two-dimensional oriented attachment. *Science* **329**, 550–553 (2010).
38. T. Taniguchi, K.-i. Katsumata, S. Omata, K. Okada, N. Matsushita, Tuning growth modes of ceria-based nanocubes by a hydrothermal method. *Cryst. Growth Des.* **11**, 3754–3760 (2011).
39. B. B. Srivastava, S. Jana, D. Sarma, N. Pradhan, Surface ligand population controlled oriented attachment: A case of CdS nanowires. *J. Phys. Chem. Lett.* **1**, 1932–1935 (2010).
40. V. Jordan, U. Javornik, J. Plavec, A. Podgornik, A. Rečnik, Self-assembly of multilevel branched rutile-type TiO_2 structures via oriented lateral and twin attachment. *Sci. Rep.* **6**, 24216 (2016).
41. G. Guo *et al.*, Self-assembly of transition-metal-oxide nanoparticle supraparticles with designed architectures and their enhanced lithium storage properties. *J. Mater. Chem. A Mater. Energy Sustain.* **4**, 16128–16135 (2016).

42. H. Wu *et al.*, Polymer-in-"quasi-ionic liquid" electrolytes for high-voltage lithium metal batteries. *Adv. Energy Mater.* **9**, 1902108 (2019).
43. W. Fan *et al.*, Synthesis, crystallization mechanism, and catalytic properties of titanium-rich TS-1 free of extraframework titanium species. *J. Am. Chem. Soc.* **130**, 10150–10164 (2008).
44. K. Qi, J. Xie, D. Fang, F. Li, F. He, Performance enhancement mechanism of Mn-based catalysts prepared under N_2 for NO_x removal: Evidence of the poor crystallization and oxidation of MnO_x. *Chin. J. Catal.* **38**, 845–851 (2017).
45. S. Niu *et al.*, Manipulating the water dissociation kinetics of Ni_3N nanosheets via in situ interfacial engineering. *J. Mater. Chem. A Mater. Energy Sustain.* **7**, 10924–10929 (2019).
46. J. Cai *et al.*, Organic additive-free synthesis of mesocrystalline hematite nanoplates via two-dimensional oriented attachment. *CrystEngComm* **16**, 1553–1559 (2014).
47. F. Montanarella *et al.*, Composite supraparticles with tunable light emission. *ACS Nano* **11**, 9136–9142 (2017).
48. C. Shao *et al.*, Repair of tooth enamel by a biomimetic mineralization frontier ensuring epitaxial growth. *Sci. Adv.* **5**, eaaw9569 (2019).
49. B. Wang *et al.*, Yeast cells with an artificial mineral shell: Protection and modification of living cells by biomimetic mineralization. *Angew. Chem. Int. Ed. Engl.* **47**, 3560–3564 (2008).
50. V. K. Ivanov, P. P. Fedorov, A. Y. Baranchikov, V. V. Osiko, Oriented attachment of particles: 100 years of investigations of non-classical crystal growth. *Russ. Chem. Rev.* **83**, 1204–1222 (2014).
51. P. Gaubert, Sur la production artificielle de la macle des spinelles dans les cristaux d'azotate de plomb. *Bull. Soc. Fr. Mineral.* **19**, 431–434 (1896).
52. L. Liu *et al.*, Connecting energetics to dynamics in particle growth by oriented attachment using real-time observations. *Nat. Commun.* **11**, 1045 (2020).
53. Y. Cheng *et al.*, Near surface nucleation and particle mediated growth of colloidal Au nanocrystals. *Nanoscale* **10**, 11907–11912 (2018).
54. M. L. Sushko, Understanding the driving forces for crystal growth by oriented attachment through theory and simulations. *J. Mater. Res.* **34**, 2914–2927 (2019).
55. M. L. Sushko, "Theoretical insight into thermodynamics of particle-based crystallization" in *Crystallization via Nonclassical Pathways Volume 1: Nucleation, Assembly, Observation & Application,* X. Zhang, Ed. (American Chemical Society, 2020), vol. 1358, chap. 5, pp. 97–114.
56. H. Zhang *et al.*, In situ synthesis of γ-AlOOH and synchronous adsorption separation of V(V) from highly concentrated Cr(VI) multiplex complex solutions. *ACS Sustain. Chem. & Eng.* **5**, 6674–6681 (2017).
57. X. Zhang *et al.*, Direction-specific interaction forces underlying zinc oxide crystal growth by oriented attachment. *Nat. Commun.* **8**, 835 (2017).
58. D. Li *et al.*, Trends in mica-mica adhesion reflect the influence of molecular details on long-range dispersion forces underlying aggregation and coalignment. *Proc. Natl. Acad. Sci. U.S.A.* **114**, 7537–7542 (2017).
59. M. J. Higgins *et al.*, Structured water layers adjacent to biological membranes. *Biophys. J.* **91**, 2532–2542 (2006).
60. D. Li *et al.*, Investigating the magnitude and source of orientation-dependent interactions between TiO_2 crystal surfaces. *Nanoscale* **9**, 10173–10177 (2017).
61. M. L. Sushko, K. M. Rosso, The origin of facet selectivity and alignment in anatase TiO_2 nanoparticles in electrolyte solutions: Implications for oriented attachment in metal oxides. *Nanoscale* **8**, 19714–19725 (2016).
62. H. Zhang, J. F. Banfield, Energy calculations predict nanoparticle attachment orientations and asymmetric crystal formation. *J. Phys. Chem. Lett.* **3**, 2882–2886 (2012).
63. H. Zhang, J. F. Banfield, Interatomic Coulombic interactions as the driving force for oriented attachment. *CrystEngComm* **16**, 1568–1578 (2014).
64. T. A. Ho, L. J. Criscenti, Molecular-level understanding of gibbsite particle aggregation in water. *J. Colloid Interface Sci.* **600**, 310–317 (2021).
65. J. S. Chen, T. Zhu, C. M. Li, X. W. Lou, Building hematite nanostructures by oriented attachment. *Angew. Chem. Int. Ed. Engl.* **50**, 650–653 (2011).
66. X. Lu *et al.*, Formation of lead ferrites for immobilizing hazardous lead into iron-rich ceramic matrix. *Chemosphere* **214**, 239–249 (2019).
67. S. R. Prim, M. V. Folgueras, M. A. de Lima, D. Hotza, Synthesis and characterization of hematite pigment obtained from a steel waste industry. *J. Hazard. Mater.* **192**, 1307–1313 (2011).
68. S. Mehdizadeh Taheri *et al.*, Self-assembly of smallest magnetic particles. *Proc. Natl. Acad. Sci. U.S.A.* **112**, 14484–14489 (2015).
69. G. Singh *et al.*, Self-assembly of magnetite nanocubes into helical superstructures. *Science* **345**, 1149–1153 (2014).
70. G. Singh *et al.*, Magnetic field-induced self-assembly of iron oxide nanocubes. *Faraday Discuss.* **181**, 403–421 (2015).
71. I. Stanković, L. Lizardi, C. García, Assembly of nanocube super-structures directed by surface and magnetic interactions. *Nanoscale* **12**, 19390–19403 (2020).
72. J.-M. Meijer, L. Rossi, Preparation, properties, and applications of magnetic hematite microparticles. *Soft Matter* **17**, 2354–2368 (2021).
73. P. U. P. A. Gilbert *et al.*, Biomineralization by particle attachment in early animals. *Proc. Natl. Acad. Sci. U.S.A.* **116**, 17659–17665 (2019).
74. W. K. Koh, A. C. Bartnik, F. W. Wise, C. B. Murray, Synthesis of monodisperse PbSe nanorods: A case for oriented attachment. *J. Am. Chem. Soc.* **132**, 3909–3913 (2010).
75. N. Pradhan, H. Xu, X. Peng, Colloidal CdSe quantum wires by oriented attachment. *Nano Lett.* **6**, 720–724 (2006).
76. A. D. Becke, Perspective: Fifty years of density-functional theory in chemical physics. *J. Chem. Phys.* **140**, 18A301 (2014).
77. E. Bylaska, K. Tsemekhman, N. Govind, M. Valiev, "Large-scale plane-wave-based density functional theory: Formalism, parallelization, and applications" in *Computational Methods for Large Systems*, J. R. Reimers, Ed. (John Wiley & Sons, Inc., 2011), pp. 77–116.
78. M. Valiev *et al.*, NWChem: A comprehensive and scalable open-source solution for large scale molecular simulations. *Comput. Phys. Commun.* **181**, 1477–1489 (2010).
79. E. Aprà *et al.*, NWChem: Past, present, and future. *J. Chem. Phys.* **152**, 184102 (2020).
80. J. P. Perdew, K. Burke, M. Ernzerhof, Generalized gradient approximation made simple. *Phys. Rev. Lett.* **77**, 3865–3868 (1996).
81. A. I. Liechtenstein, V. I. Anisimov, J. Zaanen, Density-functional theory and strong interactions: Orbital ordering in Mott-Hubbard insulators. *Phys. Rev. B Condens. Matter* **52**, R5467–R5470 (1995).
82. G. Rollmann, A. Rohrbach, P. Entel, J. Hafner, First-principles calculation of the structure and magnetic phases of hematite. *Phys. Rev. B Condens. Matter Mater. Phys.* **69**, 165107 (2004).
83. D. R. Hamann, Generalized norm-conserving pseudopotentials. *Phys. Rev. B Condens. Matter* **40**, 2980–2987 (1989).
84. N. Troullier, J. L. Martins, Efficient pseudopotentials for plane-wave calculations. *Phys. Rev. B Condens. Matter* **43**, 1993–2006 (1991).
85. L. Kleinman, D. M. Bylander, Efficacious form for model pseudopotentials. *Phys. Rev. Lett.* **48**, 1425–1428 (1982).
86. D. Meng, B. Zheng, G. Lin, M. L. Sushko, Numerical solution of 3D Poisson-Nernst-Planck equations coupled with classical density functional theory for modeling ion and electron transport in a confined environment. *Commun. Comput. Phys.* **16**, 1298–1322 (2014).